Low-level liquid-bearing clouds contribute to seasonal lower atmosphere stability and surface energy forcing over a high-mountain watershed environment

Joseph Sedlar,[a,b] Tilden Meyers[c], Christopher J. Cox[d] , and Bianca Adler[a,d]

[a] *Cooperative Institute for Research in Environmental Sciences, University of Colorado Boulder, Boulder, Colorado*

[b] *NOAA Global Monitoring Laboratory, Boulder, Colorado*

[c] *NOAA Air Resources Laboratory, Oak Ridge, Tennessee*

[d] *NOAA Physical Sciences Laboratory, Boulder, Colorado*

etc.

Corresponding author: Joseph Sedlar, joseph.sedlar@colorado.edu

ABSTRACT

Measurements of atmospheric structure and surface energy budgets distributed along a high-altitude mountain watershed environment near Crested Butte, Colorado, USA, from two separate, but coordinated, field campaigns, SAIL and SPLASH, are analyzed. This study identifies similarities and differences in how clouds influence the radiative budget over one snow-free summer season (2022) and two snow-covered seasons (2021-22; 2022-23) for this alpine location. A relationship between lower tropospheric stability stratification and longwave radiative flux from the presence or absence of clouds is identified. When low clouds persisted, often with signatures of supercooled liquid in winter, the lower troposphere experienced weaker stability, while radiatively clear skies that are less likely to be influenced by liquid droplets were associated with appreciably stronger lower tropospheric stratification. Corresponding surface turbulent heat fluxes partitioned differently based upon the cloud-stability stratification regime derived from early morning radiosounding profiles. Combined with the differences in the radiative budget largely resulting from dramatic seasonal differences in surface albedo, the lower atmosphere stratification, surface energy budget, and near-surface thermodynamics are shown to be modified by the effective longwave radiative forcing of clouds. The diurnal evolution of thermodynamics and surface energy components varied depending on early morning stratification state. Thus, the importance of quiescent versus synoptically-active large-scale meteorology is hypothesized as a critical forcing for cloud properties and associated surface energy budget variations. The physical relationships between clouds, radiation, and stratification can provide a useful suite of metrics for process-understanding and to evaluate numerical models in such an undersampled, highly complex terrain environment.

1. Introduction

The balance of incoming and outgoing radiation through Earth's atmosphere with the surface drives the weather and climate patterns across the globe. Energy to our climate system is input through shortwave (solar) radiation, interacting with atmospheric gases, aerosols, cloud hydrometeors, and ultimately with Earth's surface through multiple interactions involving scattering and absorption. The net shortwave at the surface after accounting for the extinction processes across the atmosphere and surface, including subsurface absorption, leads to temperature perturbations that ultimately impact the other surface energy budget components, including longwave (infrared) radiation, turbulent heat flux partitioning into latent and sensible heating, as well as local storage (e.g., Stull, 1988). This redistribution of radiative energy determines the near-surface forcing that drives local weather scales, and ultimately climate forcings (Peixoto and Oort, 1992). The relative importance of radiative forcing and the response of surface turbulent exchange and local storage have a great dependence on phase and size of cloud hydrometeors, the vertical location of the cloud layers (Shupe and Intrieri, 2004; Miller et al., 2015; Ceppi and Nowack, 2021), but also on the underlying surface characteristics.

Areas of Earth's surface covered by snow, glaciers, or sea ice have a higher surface albedo than open water or snow-free land surfaces (Weihs et al., 2021). When underlying surfaces are highly reflective, the relative contribution of shortwave net (SWN) and longwave net (LWN) radiation to the total net radiation (R_{net}) at the surface can vary. Over snow-free and ice-free surfaces, SWN typically dominates the total radiation over LWN. However, clouds can further impact the magnitude of the radiative flux components reaching the surface through what is known as cloud radiative forcing (Ramanathan et al., 1989). The relative radiative warming or cooling at the surface resulting from cloud radiative forcing greatly depends upon the albedo of the surface (Shupe and Intrieri, 2004; Sedlar et al., 2011; Miller et al., 2015), the phase and size of cloud hydrometeors, and the height of clouds above the surface, which impacts the ambient temperature and phase of the cloud particles (Stramler et al., 2011; Ceppi and Nowack, 2021). The lower atmospheric stratification and turbulent heat exchange respond to the cloud-induced radiative flux partitioning differently depending on surface albedo, leading to cloud-radiative induced modifications to the surface energy budget.

At high elevations and in the absence of glaciers, the optical properties of the surface change dramatically with season. Low surface albedos during the snow-free summer often abruptly change to highly reflective surfaces with the onset of winter seasonal snowpack (Marty et al., 2002). The relative contributions of SWN and LWN to total R_{net} adjust accordingly. The role of aerosol deposition in modifying surface albedo and changing ablation characteristics on high mountain snow surfaces is considered an important mechanism in determining mountain snow lifecycle (e.g., Skiles et al., 2012; 2018). However, the surface energy fluxes contributing to melt of glaciers across high-altitude mountains are often more dominated by the LWN than SWN because of the high annual glacial surface albedo limiting the absolute magnitude of SWN (e.g., Ohmura, 2001; Marty et al., 2002; Sedlar and Hock, 2009).

A geographic region with similar characteristics to the high mountain, snow-covered environment is the high-latitude Arctic Ocean. Here, the surface is frequently covered by highly reflective sea-ice and overlying snow cover and the surface energy balance (SEB) is often dominated by the longwave contribution (e.g., Intrieri et al., 2002a), especially in the absence of solar radiation during polar winter, but also during critical sunlit periods such as the onset of seasonal melt (e.g., Persson, 2012). Over Arctic sea-ice, low-level liquid-bearing clouds frequently exert a positive cloud forcing and thus warm the surface (Walsh and Chapman, 1998; Shupe and Intrieri, 2004; Sedlar et al., 2011). The cloud layer blankets the lower atmosphere, limiting the escape of upwelling longwave to space and reduces the deficit in surface LWN. Resulting in part from the surface cloud warming effect, the near-surface stability stratification can be modulated (Sedlar et al., 2011; Shupe et al., 2013; Sedlar and Shupe, 2014; Sotiropoulou et al., 2016), which can prevent the development of strong, surface-based stable layers often associated with clear sky conditions or conditions when ice crystals represent the primary cloud phase. Clouds found across the lower atmosphere (below 3000 m above surface) commonly have a sub-cloud static mixed layer driven by radiative divergence across the cloud layer (e.g. Paluch and Lenschow, 1991), which further modulates the stratification of the lower Arctic atmosphere where they typically form (Shupe et al., 2008; 2013; Sedlar and Shupe, 2014; Brooks et al., 2017). Stability modifications are important for the magnitude and direction of turbulent heat fluxes and can potentially feedback onto the evolution of lower atmosphere cloud cover (Sedlar and Shupe, 2014). These cloud-stability relationships can precondition the surface through near-surface temperature modifications, further exacerbating the stratification as well as contributing to snow and ice melt through anomalies in the SEB. Whether similar responses of the lower atmosphere to clouds over a high-altitude mountain seasonal snowpack exist has yet to be investigated.

The high-altitude Colorado Rocky Mountain environment experiences drastic seasonal shifts through the presence and absence of seasonal snow cover. The characteristics of the surface in turn alter the relative importance of the different energy components that contribute to the local SEB (Adler et al., 2023). In this study, observations from the Department of Energy's Surface Atmosphere Integrated field Laboratory (SAIL; Feldman et al., 2023) and NOAA's Study of Precipitation, the Lower Atmosphere, and Surface for Hydrometeorology (SPLASH; de Boer et al., 2023) combined field campaigns in the upper East River Valley of the Rocky Mountains near Gothic, Colorado, are investigated. A multivariate observational metric relating measurements of LWN and near-surface stability from sounding profiles (Sedlar et al., 2020) is employed to infer the aforementioned relationships for two distinctly different high-mountain seasons, the snow-free summer and snow-covered winter. This study is motivated by many years of studies that have linked the importance of liquid-bearing clouds to the SEB and atmospheric stratification of Arctic sea ice to understand whether or not similar relationships between clouds radiation, and stratification exist for different high-mountain seasons during SPLASH and SAIL campaigns. The observations and calculations are described in Section 2. Results are presented and discussed throughout Section 3, while Section 4 provides a summary of the main findings.

2. Data and methods

To study the interactions and responses of the atmosphere in a high-mountain watershed environment, observations in the upper East River valley began in September 2021 for the SAIL campaign (Feldman et al., 2023) through the deployment of the Atmospheric Radiation Measurement (ARM) Mobile Facility (AMF2) near Gothic, Colorado. The overarching science goals of the combined SAIL-SPLASH field campaign revolve around improved monitoring of precipitation and understanding how the atmosphere and surface processes interact to support and feed the hydrology of this critical mountain watershed environment (Fig 1a-b). The AMF2 deployed a number of in situ and remote sensing instruments that probe turbulence, cloud properties, surface energy fluxes, and aerosols from the surface through the troposphere. The extensive SPLASH field effort began approximately one month later but deployed at five locations across the East River valley (Fig. 1b). A range of radiation, turbulence, and remote sensing measurements were deployed at these sites. This study uses a combination of ARM-AMF2 and NOAA Global Monitoring Laboratory and NOAA Air Resources Laboratory observations from two nearby stations, Gothic and Kettle Ponds (Fig 1c). At Kettle Ponds, broadband radiometer (Soldo et al., 2023) and ceilometer (Telg et al., 2024) instruments provide measurements of shortwave and longwave radiative fluxes and cloud fractional and cloud base height. All radiative fluxes are positive for a surplus of energy at the surface. Eddy covariance processing techniques were applied to high-frequency 3-D sonic anemometer, sonic temperature, and open-path gas analyzer measurements to estimate turbulent heat fluxes at a nominal height of 3 m AGL; turbulent heat fluxes are defined positive from the surface to the atmosphere. Radiosoundings were launched nearby Gothic nominally twice per day (00:00/12:00 UTC, nominally 17:00/05:00 LST), providing tropospheric profiles of thermodynamics and wind (Atmospheric Radiation Measurement (ARM) user facility, 2021a). Retrievals from a dual channel microwave radiometer (MWR) (Atmospheric Radiation Measurement (ARM) user facility, 2021b) provide information on the presence of cloud liquid water path (LWP) integrated vertically through the troposphere (e.g., Westwater et al., 2001). Profiles of aerosol and cloud particulate backscatter and depolarization ratio from the High Spectral Resolution Lidar (HSRL; e.g., Eloranta, (2005)) provide additional information related to the size and phase of the hydrometeors near the observed cloud base height (Atmospheric Radiation Measurement (ARM) user facility, 2023). A detailed description of the scientific rationale for all measurements, including their spatial-temporal distributions, can be found in Feldman et al. (2023) for SAIL and de Boer et al. (2023) for SPLASH. See Data Availability statement below for references to data sets used.

This study analyzes quality-assessed datasets from both SAIL and SPLASH from mid-October 2021 through early May 2023. The SAIL campaign officially concluded its measurement phase in June 2023, while the NOAA measurements continued sampling until late summer/early autumn 2023, staggering between the different NOAA labs. Due to differences in measurement end dates, the relationships between the SEB, clouds, and lower atmospheric stability are split into two seasonally snow-covered winter seasons (2021-22 and 2022-23) and one seasonally snow-free summer season (2022); measurements from the two winters are combined in subsequent analyses as the winter season.

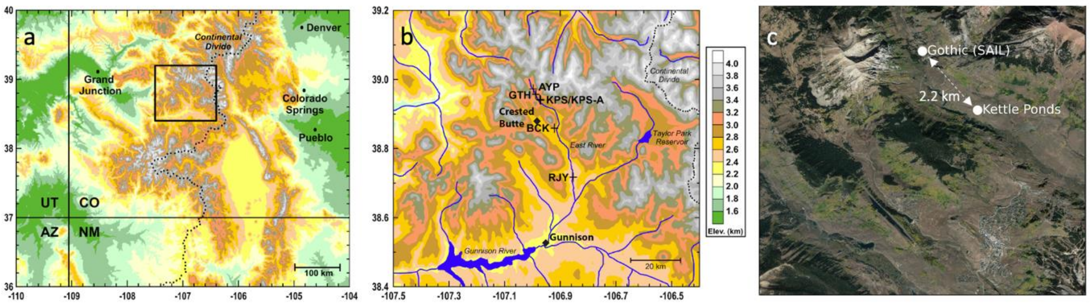

Fig. 1. a) Broad spatial map highlighting the Continental Divide of the Rocky Mountains and the East River/Gunnison River Watershed region. b) Broader view of the East River Watershed and spatial extent of SPLASH and SAIL (GTH – Gothic) observation stations. c) Satellite view of the Gothic (SAIL) and Kettle Ponds observation stations used in this study. Adapted from Fig. 1 in de Boer et al. (2023).

Rather than separate summer and winter seasonality by traditional meteorological seasons (i.e., DJF, JJA), we adopted an approach that used the large temporal changes of calculated surface albedo at Kettle Ponds to define seasons (Fig. 2a). Seasonally persistent snowpack commenced around 12 December 2021 and remained present until mid-April 2022. To avoid contaminating the winter period with melting and patchy snowpack, 5 April 2022 was chosen as the end of winter 2021-22. Persistent snowpack for the following winter 2022-23 season also commenced in early December 2022. Compared to the previous winter, winter 2022-23 received an exceptionally high snowfall and snowpack actually surpassed the measurement height of the upwelling radiation measurements located about 1.5 m AGL. This resulted in an artificial surface albedo near zero from mid-March to mid-April 2023; this time period has thus been removed from the albedo record in Fig. 2a. We therefore define the end of winter 2022-23 to be due to 10 March 2023. For the snow-free summer 2022, we excluded the transition periods with patchy snow cover and defined summer to be 03 May 2022 to 15 October 2022. Transitions in near-surface temperature around local solar noon time generally correspond well with these definitions of seasons (Fig. 2b), reflecting the importance of seasonal albedo influence on the SEB. Changes in the boundary layer thermodynamic structure during the transition from snow-free autumn to winter seasonal snowpack in 2021 to early 2022 (Adler et al., 2023) highlight further the importance of seasonal albedo. These two winter seasons experienced similar albedo magnitudes and temporal evolution. Therefore, for analysis both winters are combined into one winter season facilitating a comparison of the process relationships between winter and summer. Note the albedo measurements are point measurements and are therefore considered representative of the local surface and not necessarily of the greater East River Valley, sloping mountain faces, or nearby forested areas.

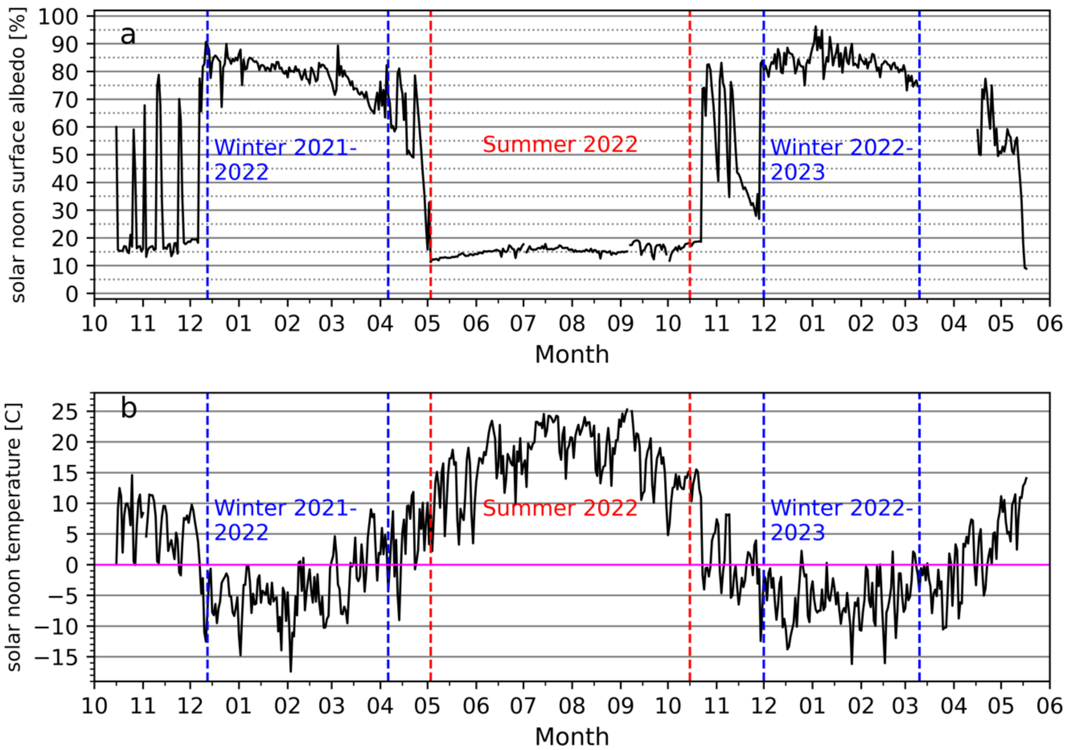

Fig. 2. Evolution of a) surface albedo (%) and b) near-surface temperature (°C) daily at local solar noon at Kettle Ponds. Observations start October 2021 through mid-May 2023. Blue and red dashed lines indicate the seasonal boundaries of the snow-covered winter 2021-22 and 2022-23 seasons and snow-free summer 2022 season, respectively. Snow pack exceeded the measurement height of the upwelling radiometers from mid-March to mid-April 2023 and thus the albedo record during this period has been removed.

Seasonal differences in the fluxes of SWN and LWN are readily identifiable through frequency distributions of each (Fig. 3a-b). Lower surface albedo during summer contributes a flat distribution, while the winter SWN distribution has a defined peak near 50 W m^{-2} and narrower tail. Warmer surface skin temperatures resulting from enhanced SWN leads to enhanced emission of upwelling longwave, following the Stefan-Boltzmann relationship

$$LW = \sigma \varepsilon T^4 \qquad (1)$$

where σ is the Stefan-Boltzmann constant (approximately 5.67×10^{-8} W m^{-2} K^4) and ε the broadband infrared emissivity. Because the outgoing LW is proportional to the 4^{th} power of temperature, T, the consequence of a warmer surface is larger for LWN deficits under clear skies (Fig. 3b). Despite the relatively large LWN deficits, the amount of SWN far exceeds the LWN under summer snow-free conditions. In winter when the surface is seasonally snow-covered, SWN and LWN are more comparable in magnitude, and the relative importance of the longwave component increases compared to a snow-free surface. Bimodal peaks in the distribution of LWN are common with a snowpack, closely resembling the bimodal behavior of radiative clear (LWN < -40 W m^{-2}) and radiatively cloudy (LWN > -20 W m^{-2}) states found during the Arctic winter (Stramler et al., 2011; Morrison et al., 2012; Engström et al., 2014).

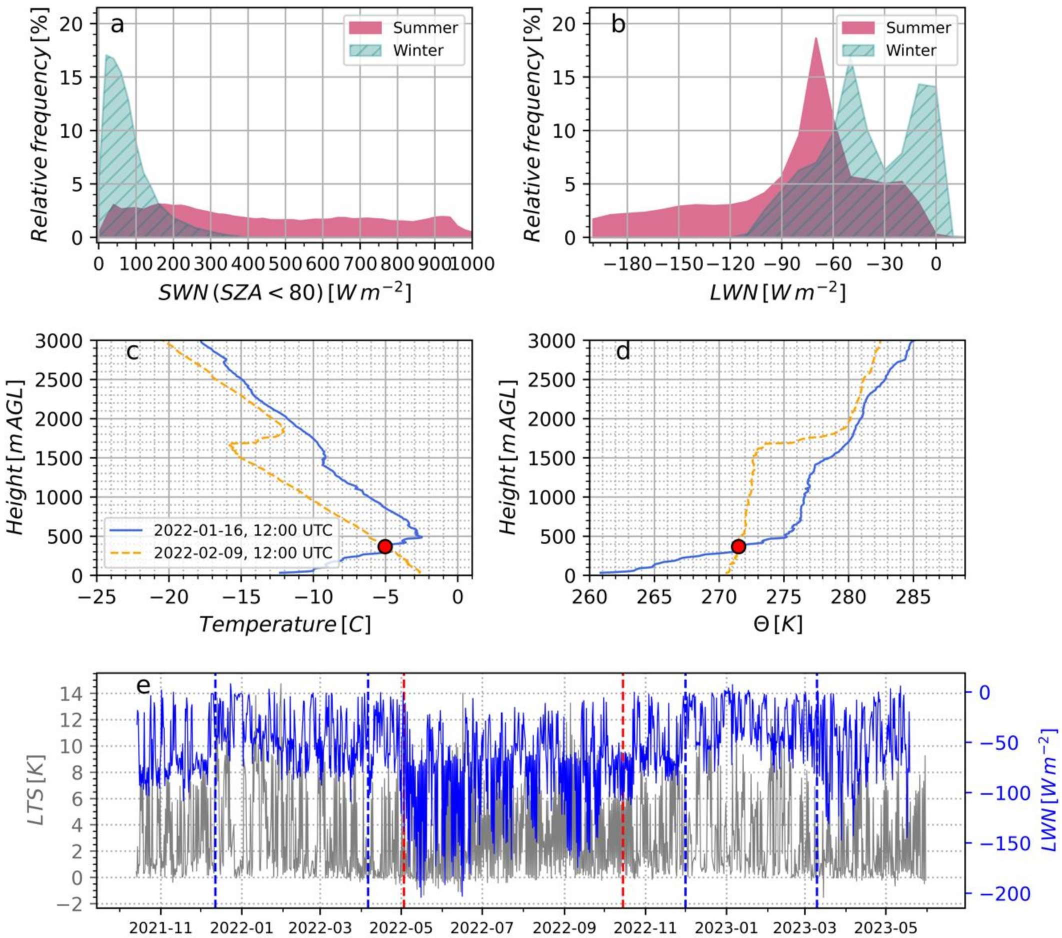

Fig. 3. Relative frequency distributions of 1-min a) net shortwave (SWN) and b) net longwave (LWN) radiation separated by summer (maroon) and winter (hatched teal). Radiosounding profiles of c) temperature (°C) and d) potential temperature (Θ, K) with height (above ground level) for two example morning 12UTC (05:00 LST) profiles. The red circles represent the pressure level 30 hPa less than the near-surface atmospheric pressure. e) Evolution of lower tropospheric stability (LTS, K) calculated from each radiosounding profile in gray, and mean LWN within 10 minutes of sounding profile launch in blue. All radiation units are W m^{-2} and defined positive from the atmosphere to the surface.

To examine how radiation and lower tropospheric stability (LTS) are related, a method proposed by Sedlar et al. (2020) and modified from Wood and Bretherton (2006) is applied. Profiles of potential temperature (Θ) are computed from radiosounding thermodynamic profiles. Two example profiles of temperature and Θ from early morning winter soundings at SAIL are shown to highlight two very different lower atmosphere stability stratification regimes (Fig. 3c-d). As Θ is conserved during adiabatic air parcel motions, a well-mixed Θ profile is approximately uniform with height, while enhanced static stability is associated with profiles where $d\Theta/dz > 0$ K m^{-1}. Seen in the January sounding (Fig. 3c-d blue), a strong surface-based temperature inversion up to ~500 m AGL was observed. The February profile (Fig. 3c-d orange) contained a lapse rate that was nearly adiabatic and therefore a near-neutral or slightly stable stratification existed up to 1500 m AGL.

Profiles of Θ were used to compute LTS metric, defined as the difference in Θ from near-surface (nominally 20 m AGL) to the pressure level that was 30 hPa below the near-surface pressure

$$LTS = \Theta(P_{sfc}\text{-}30hPa) - \Theta(P_{sfc}) \qquad (2)$$

LTS is computed for all available radiosounding profiles, providing a time series of a twice daily metric of lower tropospheric bulk layer stability. Because LTS is computed through a layer approximately 300 m thick, the metric estimates the stratification across a deeper lower atmosphere layer and may not always reflect sharp gradients across a thin geometric layer just above the surface. The evolution of LTS during the field campaign (Fig. 3e gray) reveals a wide range of variability, from very strongly stable (> 12 K) to very near-neutrally stratified (0 K) conditions (Fig. 3e). Overlaid with LTS is the evolution of averaged LWN value calculated within 10 minutes of each sounding (blue). A great deal of variability in LWN is also observed, diurnal as well as seasonally, which is reflected in the distributions of Fig. 3b. While difficult to discern from the time series comparisons, a relationship between LWN and LTS occurs, such that when LWN deficits were small (near 0 W m^{-2}), LTS tended to also be small (i.e., around January 2022). The opposite is found for large, negative values of LWN (large deficits, e.g. February 2023). This relationship is consistent with results found for lower atmosphere stratification over Arctic sea ice (Sedlar et al., 2020), motivating the subsequent analyses related to the role that cloud cover and surface state have on atmospheric stratification. The measure of LTS reflects stratification of a deeper layer than the near surface-layer gradient stability, allowing us to isolate the potential impact of cloud-radiative forcing on the lower atmosphere stratification as opposed to the sharp gradients introduced by surface-air interface differences in temperature.

3. Results

a. Radiation-stability regimes

Relative frequency distributions of LWN against LTS calculated for all soundings during the period of analysis indicate a complex, multi-clustered relationship between stability and longwave radiation (Fig. 4a). Clusters of observations within the distribution suggest radiation-stability regimes are identifiable through this relationship.

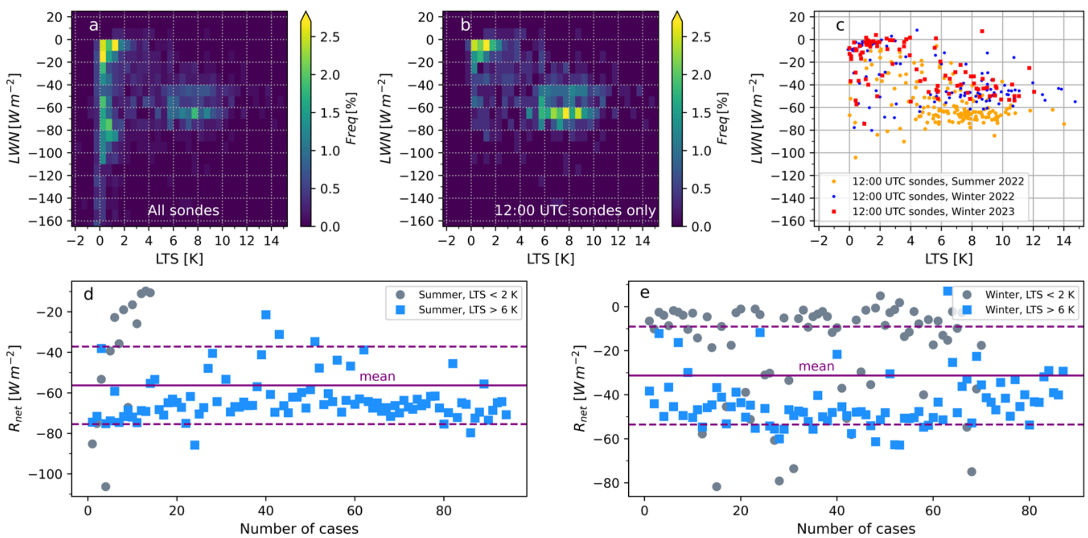

Fig. 4: a-b) Relative frequency distributions (RFDs, colors (%)) for LWN (W m^{-2}) vs. LTS (K) phase-space relationships for a) all sounding profiles; b) only 12:00 UTC (~05:00 LST) sounding profiles; c) scatter plot of LWN vs. LTS from 12:00 UTC soundings separated by Summer 2022 (orange), Winter 2021-22 (blue), and Winter 2022-23 (red). d-e) Mean and 1-σ (solid and dashed purple lines) of net radiation (R_{net}, W m^{-2}) within 5 min of each morning 12 UTC sounding for the d) snow-free and e) snow-covered seasons. Symbols represent anomalies in R_{net} (relative to the seasonal mean value) when morning sounding LTS < 2 K (gray circles) and when LTS > 6 K (blue squares).

The clustering of observations can be separated by stability strength, either less stable (LTS < 2 K) or more (referred to also as strongly) stable (LTS > 6 K), as well as by LWN deficit (0 W m^{-2} > LWN > -20 W m^{-2} and LWN < -40 W m^{-2}). The more stable regime was associated with deficits in LWN centered around -65 W m^{-2}. Maximum LWN rarely exceeded -40 W m^{-2} for this subset of observations. The other less stable regime (LTS < 2K) could be further separated into two sub-groups based on the LWN deficit. One had LWN observations clustered near -10 W m^{-2} with the majority deficits above -20 W m^{-2}. For a LWN deficit of this magnitude, the upwelling longwave (LWU) and downwelling longwave (LWD) radiation are very similar. This suggests the presence and radiative forcing of cloud cover causes similar effective infrared emission temperatures of the surface and atmosphere. The second of the less stable clusters shows much larger LWN deficits, centered around -80 W m^{-2} but occasionally below -100 W m^{-2}.

The distribution of clustering in the LWN vs. LTS phase space changes when only considering the early morning 12:00 UTC radiosounding profiles (Fig. 4b). Two distinct regimes are present, the less stable (LTS < 2 K, LWN > -15 W m^{-2}) and the strongly stable regime (LTS > 6 K, LWN ~ -65 W m^{-2}). Because soundings were launched locally early in the morning or early in the evening, the ability to separate regimes temporally supports a connection in the diurnal evolution of the stratification. Minimum temperatures are typically observed just before sunrise because net radiation is only affected by LWN. Often surface-based temperature inversions form as the surface loses longwave radiative energy to the atmosphere, resulting in high static stability across the lower atmosphere. However, a relatively large number of 12:00 UTC morning soundings still clustered around less stable stratification, indicating at least one component of the surface energy budget inhibited runaway surface longwave cooling. Likewise, the disappearance of the sub-group of less stable stratification under large LWN deficits from the morning-only distribution indicates this regime is a function of a daytime surface heating (larger LWN deficit) and surface-based convection (Adler et al., 2023). Beyond diurnal sampling, the seasonal state of the surface as either snow-free or snow-covered generally did not favor one LWN-LTS regime over another (Fig. 4c). While the less stable regime was overly common in summer, both it and the strongly stable stratification regime were present during the two winter seasons. It is seen that during the summer, higher LTS were associated with larger LWN deficits than those for stable cases in winter. These temporal and surface characteristics suggest surface skin temperature differences between snow-free and snow-covered surfaces impact the surface LWU through the Stefan-Boltzmann relationship on emission temperature.

These relationships indicate that stratification of the lower troposphere has a unique dependency on the longwave radiation characteristics of the surface and atmosphere. To connect the surface R_{net} budget to these LTS states, anomalies in R_{net} for the two bulk stability states are inferred by comparing to the average R_{net} (± 1-σ) for both summer (Fig. 4d) and winter (Fig. 4e) in a 15 min window following 12:00 UTC. The impact of a warmer surface and larger LWU for summer versus winter is evident by comparing the change in mean R_{net} of ~ -60 W m^{-2} to ~ -30 W m^{-2}, respectively (purple lines). When comparing stability regimes, the majority of the less stable cases were associated with R_{net} above -20 W m^{-2}, and frequently above -10 W m^{-2} in winter (gray circles in d-e). Note for summer, the LTS < 2 K regime only had 14 identified occurrences; therefore, statistics for this regime are biased by fewer observations. Relative to the means for each season, the weaker stratification regime contributed significantly (at or exceeding 1-σ over the mean) to the R_{net} budget through anomalies ranging from +20 to +40 W m^{-2}. On the other hand, the highly stratified cases (blue squares in Fig. 4e-f) were typically associated with R_{net} anomalies of 5 to 20 W m^{-2} below average, although most cases were within the variability of 1-σ of the mean and thus not significantly anomalous.

b. Cloud characteristics and the separability by radiation-stability regime

Over Arctic sea ice, LWN-LTS regime relationships are dependent on the presence (or absence) of low-level liquid bearing clouds (Sedlar et al., 2020). When containing liquid droplets, cloud cover is extremely efficient in absorbing LWU and emitting that back to the surface (Stephens, 1978a). Similarly, stratification of the lower Arctic atmosphere is often controlled by whether liquid-containing clouds exist (Shupe et al., 2013; Sedlar, 2014; Sedlar and Shupe, 2014; Brooks et al., 2017). Here, the occurrence of cloud cover and the vertical distribution of clouds, which provides an indication on the infrared emission temperature, during the two stratification regimes are examined.

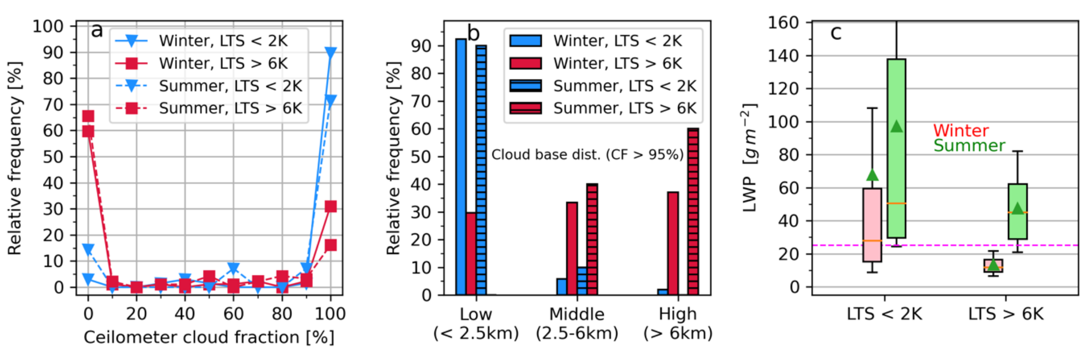

Fig. 5: a) Relative frequency of ceilometer-derived mean cloud fraction within 15 min of 12:00 UTC sounding by stability regime, where LTS < 2 K (less stable, blue triangles) and LTS > 6K (more stable, red squares) and season (winter in solid, summer in dashed). b) Relative frequency of overcast (cloud fraction > 95%) cloud base height AGL (low, middle, high) by stability regime and seasons (winter in solid, summer in hatched) determined from 12:00 UTC soundings. c) box-whisker distributions (10th-90th, 25-75th, median [orange line], mean [green triangle]) of retrieved LWP (g m^{-2}) from the MWR within 15 min of 12:00 UTC sounding separated by stability regime and season (winter in pink, summer in green); magenta dashed line indicates the LWP retrieval uncertainty for the MWR.

A distinct separation in cloud fractional occurrence calculated from the Kettle Ponds ceilometer cloud base identification between early morning stability regimes is observed over the high-mountain watershed (Fig. 5a). Outside of some infrequent broken cloudiness, the less stable regime (blue) was coincident with high temporal cloud fractions indicative of overcast cloud cover. Oppositely, the more stable regime (red) was dominated by clear skies albeit winter saw an increase in 100% cloudiness compared to summer. To first order, the presence or absence of cloud cover corroborates the distinction between "radiatively cloudy" and "radiatively clear" surface longwave radiative states, respectively (Stramler et al., 2011). Focusing only on cases when the early morning LTS state was influenced by overcast cloudiness (>95% cloud fraction), a stark separation between the vertical location of the cloud base height exists for the two regimes (Fig. 5b). In both seasons, low clouds dominated the less stable regime, while mid to high clouds were observed most frequently when under strong stability. Following the atmospheric lapse rate, clouds found lower in the troposphere are often warmer than higher level clouds. By this argument, the infrared emission temperature would be warmer for lower clouds, contributing to enhanced LWD relative to cooler, higher cloud base temperatures. Cloud base temperature differences are investigated further in the next subsection.

Because cloud infrared emissivity increases exponentially with cloud liquid water path (LWP) (Stephens, 1978b), retrievals of LWP are examined to distinguish the presence of supercooled cloud liquid. Box-and-whisker distributions of LWP were greater for the early morning LTS < 2K regime compared to the LTS > 6K regime (Fig. 5c). The MWR retrievals have a reported uncertainty of nearly 25 g m^{-2} (Westwater et al., 2001), thus clouds with LWP estimates under 25 g m^{-2} cannot, with certainty, be considered to bear liquid droplets. This is the case for the narrow LWP distribution for winter under strong stability. However, given the LWP distributions exceed the retrieval uncertainty for at least the 50th percentile during winter (even larger during summer), it is highly likely supercooled liquid was present within the clouds during the less stable regime. This stability regime likely occurs when clouds are low and contain sufficient LWP to enhance infrared emissivity and enhanced surface flux of LWD. A cloud with LWP increasing from near zero to 10 g m^{-2} can cause an exponential increase in infrared emissivity from about 0.2 to 0.8 (Sedlar, 2018). Due to this increasing emissivity, additional downwelling longwave flux ranging from 30 to 40 W m^{-2} could be expected, representing a significant amount of radiative forcing similar in magnitude to the differences associated with stratification shown in Fig. 4e.

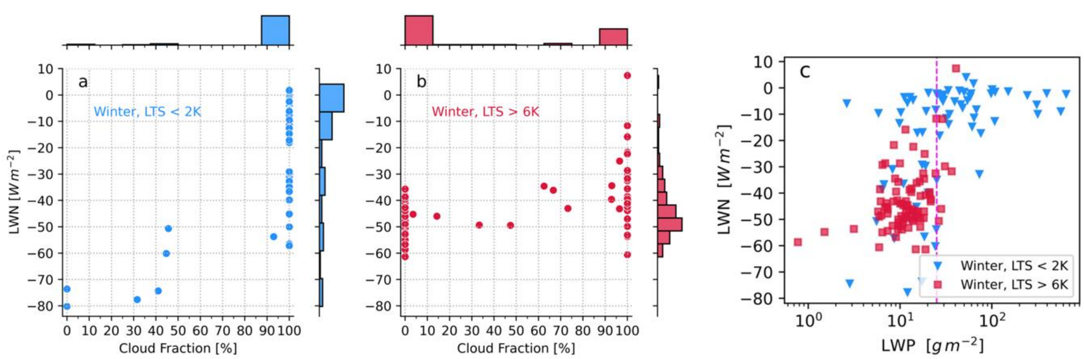

Fig 6. a-b) Scatter plot of winter-only LWN [W m^{-2}] as a function of cloud fraction [%] observed at time of early morning stability classification regime for a) the weakly stable (LTS < 2K) and b) strongly stable (LTS > 6K) cases. The bars on the top and right axes in a-b) represent the relative number of cases in each LWN-cloud fraction pairing. c) Scatter plots by stability regime of LWN as a function of retrieved LWP [g m^{-2}] from the MWR. The vertical magenta line indicates the 25 g m^{-2} retrieval uncertainty value for LWP.

To further examine the potential for cloud longwave forcing contributing towards a specific LTS regime, we focus on some macrophysical properties of winter-season-only clouds. Regarding cloud fraction and LWN, a tight relationship between the two is evident in the regime scatter plots (Fig. 6a-b). Overcast conditions associated with a mode of LWN > -20 W m^{-2} occurred most frequently with the less stable regime. As expected from LWP results shown in Fig. 5, this mode of LWN is most often coincident with LWPs above the MWR retrieval uncertainty amount of 25 g m^{-2} (Fig. 6c). An asymptotic behavior of LWN near 0 W m^{-2} with increasing LWP provides evidence that some of these clouds are at or approaching an emissivity of unity, or blackbody clouds (Curry et al., 1996; Shupe and Intrieri, 2004; Sedlar et al., 2011), making these clouds very effective in trapping outgoing longwave and emitting back to the surface. The distributions are slightly different under the more stable regime, where most early mornings within this regime are cloud free (Fig. 6b). LWN during these clear sky conditions generally scatter around -50 W m^{-2} (Fig. 6c), well capturing a "radiatively clear" state. When clouds were present, LWN increased to a range of -50 to -30 W m^{-2}, although still lower than the "radiatively cloudy" LWN mode of > -20 W m^{-2}. The LWPs associated with LTS > 6K cases were almost universally below the retrieval uncertainty (Fig. 6c). Considering theses larger LWN deficits, the presence of cloud liquid is not anticipated in these clouds. Interestingly, a similar LWN mode at 100% cloud fraction and with LWN < -30 W m^{-2} also occurs for the less stable regime (blue), although it's not a frequently observed mode of the distribution. The LWPs retrieved with this LWN regime tend to bunch with the LTS > 6K regime and further suggest a minority presence of "radiatively clear" cloud conditions also for the less stable cases.

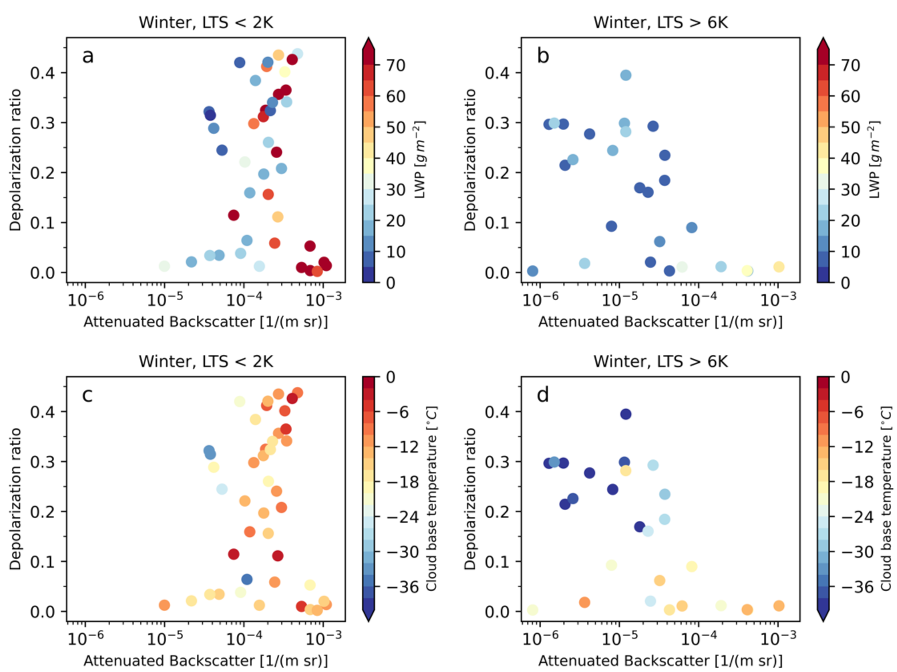

Fig. 7. Winter-only relationships between HSRL depolarization ratio (unitless) and hydrometeor backscatter [1 (m sr)$^{-1}$] observed at cloud base height for the cloud layer present at the time of early morning LTS regime classification: (a, c) for weakly stable (LTS < 2K) and (b, d) for strongly stable (LTS < 6K) regimes.

Relationships between the backscatter attenuation and depolarization ratio from the HSRL are investigated to gain insight into the phase preference of clouds between the two LTS regimes. The depolarization ratio and backscatter relations are supplemented with LWP (Fig. 7a-b) and cloud base temperature (Fig. 7c-d) contouring to further analyze the likelihood for cloud liquid; cloud base temperature determined is the radiosounding temperature at cloud base height. Lidar returns are dependent on the size and phase of the hydrometeors. Often in polar studies of mixed-phase clouds, those with liquid present tend to have a high attenuated backscatter cross-section (> $2x10^{-5}$ [m^{-1} sr^{-1}]) while the depolarization ratio is often low, typically below 0.1 (e.g., Intrieri et al., 2002b; Shupe, 2007; Inoue and Sato, 2023).

Comparing the two LTS regimes, there is an obvious separability in the attenuated backscatter where most weaker stability cases have backscatter > $1x10^{-4}$ m^{-1} sr^{-1} while the majority of backscatter for the more stable cases are < $1x10^{-4}$ m^{-1} sr^{-1}. The larger cross-sectional area lends evidence to the potential of increased opacity of the cloud, potentially resulting from more prevalent liquid hydrometeors (Shupe, 2007) when LTS < 2K. With both LTS regimes, a fraction of the cloudy cases did occur at relatively high backscatter and low (< 0.1) depolarization ratio. The LWPs for these clouds were often at or above the 25 g m^{-2} retrieval uncertainty (Fig. 7a-b) and cloud base temperatures were relatively (>-15ºC) warm (Fig. 7c-d). Thus, the presence of supercooled is highly likely for these clouds in this depolarization-backscatter grouping.

However, depolarization ratios were not exclusively below 0.1 for either regime but instead the majority were well above this characterized upper limit for cloud liquid (Intrieri et al., 2002b; Shupe, 2007; Inoue and Sato, 2023). Several of the LTS < 2K cases with larger depolarization ratio (> 0.1) were associated with LWP > 25 g m^{-2} together with generally warmer cloud base temperatures, suggesting liquid may still be present in these clouds. The dominance of larger depolarization ratios however does indicate that snow and/or ice crystal precipitation may be dominating the lidar signal near cloud base. That the depolarization ratios remain large indicates these clouds are different in microphysical composition to polar mixed-phase stratocumulus, where cloud liquid is generally found to be relatively stable at cloud top with light ice crystal precipitation into the sub-cloud layer below (Intrieri et al., 2002b; Shupe et al., 2008). For the less stable regime, the dominance of ice and/or snow determined from depolarization ratios suggests this regime may be supported by larger-scale meteorological forcing, potentially contributing to warmer atmospheric temperature advection and synoptical ascent needed to maintain some presence of cloud liquid all the while supporting ice/snow near cloud base. Oppositely, the reduction in HSRL backscatter, combined with large depolarization ratios, very small LWPs, and colder base temperatures with the strongly stable LTS > 6K regime indicate these cloudy cases are likely higher, more optically thin, ice clouds. Such a cloud regime is more similar to the "radiatively clear" classification, likely explaining the lack of observed LWN greater than -30 W m^{-2} for this overcast cloud regime (Fig. 6b).

To further test if cloud liquid could explain the separation in LWN between LTS regimes, estimates of LWD due solely to clouds consisting of liquid-only are computed through the Stefan-Boltzmann relation (Eqn. 1). Infrared emissivity (ε) is approximated using an exponential relationship, $\varepsilon = 1 - e^{-a_0 \cdot LWP}$, where a_0 is the mass absorption constant 0.158 m^2 g^{-1} (Stephens, 1978b). Assuming the radiosounding cloud base temperatures are close to the actual cloud emission temperature, LWD is computed and can be compared to observations to determine whether a liquid-bearing cloud layer could have been responsible for the observed LWD flux. Note this estimate only considers radiation being emitted from the cloud layer as there is no atmospheric contribution to LWD in this calculation.

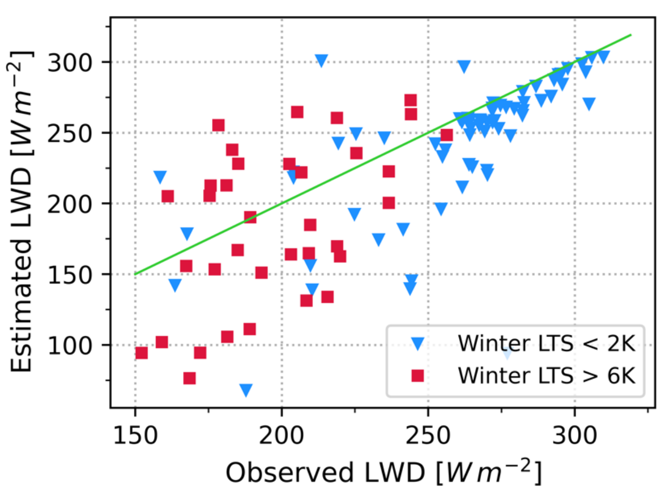

Fig. 8. Comparison of estimated LWD [W m^{-2}] against the observed LWD at the time of stability regime classification from the early morning sounding for winter season only. Weakly stable regime (LTS < 2K) in blue triangles, strongly stabile regime (LTS > 6K) in red squares. Estimated LWD is computed using the Stefan-Boltzmann relation with effective emissivity estimated using Stephens (1978b) parameterization described in the text. Green line represents the 1:1 line.

Figure 8 shows the relationship between estimated and observed LWD. Only cases where a LWP retrieval was available and cloud base height from ceilometer was observed to find the radiosounding cloud base temperature are included. While significant scatter is found for both LTS regimes, 62% of estimated LWD for weakly stable regime were within +/- 20 W m^{-2} of the observed value with nearly all these estimates only slightly below the 1:1 line. Considering there is no atmospheric component contributing to the calculated flux, it is very likely the MWR LWPs during these cloudy cases were indeed retrieving actual cloud liquid and the supercooled clouds were responsible for the enhanced LWD flux. For the strongly stable regime, only 8 (22%) of the estimated LWD calculations were within 20 W m^{-2} of the observed; the majority were scattered both well above and well below the observed flux. The large overestimated LWDs are likely to occur when 1) the MWR retrieval suggested LWP but no liquid was actually present (within the instrument retrieval uncertainty); or 2) the cloud base temperature is not representative of the infrared emission temperature, or a combination of both. These cases are likely to occur when the cloud layer is optically thin in the infrared, which would occur for an ice-phase cloud. The calculations that largely underestimated the LWD fluxes are likely a result of assuming the cloud layer is emitting all the flux and not including the atmospheric contribution to the calculation. As noted, both LTS regimes had some underestimated outliers, indicating that ice-phase clouds were likely present during both regimes (see Fig. 7) but were the minority when LTS < 2K.

c. Radiation and near-surface temperature

In this section, the relationships between radiation and near-surface temperatures for the different stability regimes by season are examined using scatter plots. Statistically significant differences in the amount of LWD were observed for the two early morning LTS regimes (Fig. 9a-b). Note, the stability regime means (large symbols in Fig. 9) calculated for both scatter plot variables for each season were statistically significantly different at, at a minimum, the 98% confidence level using a two-sided Student's T-test. Regime means differed in LWD by 30 W m^{-2} in summer to over 70 W m^{-2} in winter (Fig. 9a-b). As LWD from the atmosphere increases, the cooling rate at the surface is reduced and LWU correspondingly increases; this is especially apparent between stability regimes during winter (Fig. 9b). Since longwave flux is proportional to the emission temperature through the Stefan-Boltzmann relation, we estimate the infrared skin temperature at the time of the early morning 12:00 UTC sounding following

$$T_{skin} = \left[\frac{(LWU-(1-\varepsilon)\cdot LWD)}{\sigma\cdot\varepsilon}\right]^{1/4} \qquad (3)$$

using the mean LWU and LWD (black circles/squares in Fig. 9a-b) and assuming ε=0.97 for a snow-free vegetated summer surface (Jin and Liang, 2006) and ε=0.985 for a snow-covered winter surface (Miller et al., 2015). The differences in mean LWU for the two stability regimes correspond with T_{skin} differences of approximately 2°C during summer and a staggering 13°C during the winter. The observed anomalies in LWD are therefore crucial in modifying the surface temperature especially during the winter with persistent snowpack.

The influence LWD anomalies have on near-surface diurnal minima (T_{min}) and maxima (T_{max}) air temperature in the 12-hour period following the morning radiosounding are examined in Fig. 9c-d. Summer T_{min} ranges were similar regardless of stability regime (Fig. 9c). But in winter, T_{min} under strong stability were most often cooler than the less stable regime (Fig. 9d). This ~10ºC difference between wintertime mean T_{min} is very similar to the estimated skin temperature differences of 13ºC computed from Eqn. 3. However, even though the more stable regime began the day considerably colder than less stable during winter, the following mean daytime T_{max} warmed to nearly equal between the two regimes; the result is opposite during summer where T_{max} was significantly warmer when preceded by strong morning stratification (Fig. 9c). Therefore, warmer early morning temperatures associated with the less stable regime (i.e., suppressed development of the inversion) in winter did not predispose the following daytime temperature to dramatically increase like was the case for the more stable regime. This is physically consistent with the influence of cloud cover on surface radiation, since the less stable regime is associated with higher cloud occurrence that both insulates the surface from cooling at night but also shades the surface from solar warming during the day.

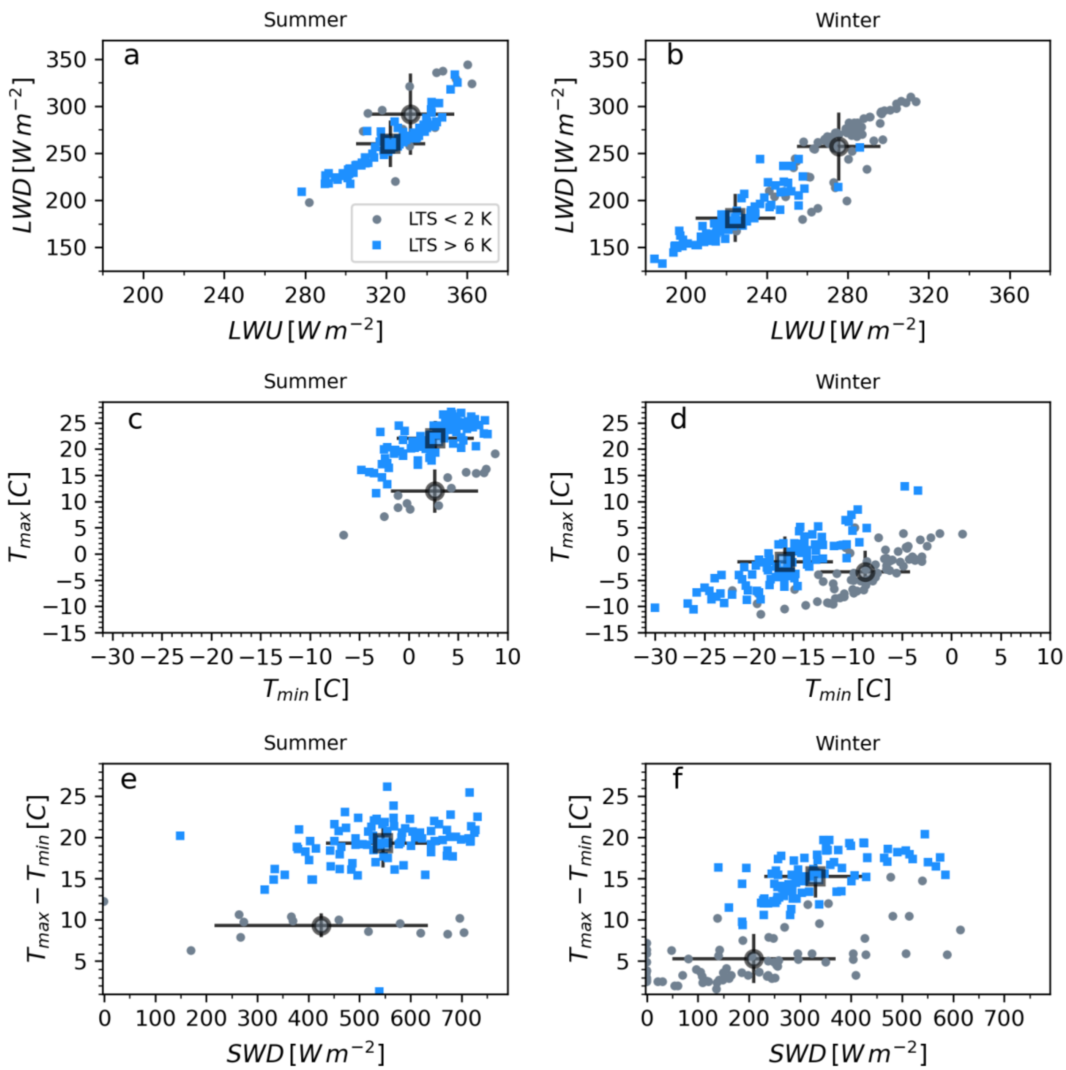

Fig. 9. Relationships between a-b) LWD and LWU (both in W m^{-2}); daytime T_{max} and morning T_{min} (ºC); and T_{max}-T_{min} diurnal amplitude and SWD (W m^{-2}) by stability regime (LTS < 2 K in gray circles, LTS > 6 K in blue squares). Data are separated by summer (a, c, e) and winter (b, d, f) seasons. Stability regime distribution means (1-σ) are shown as large black symbols (lines). Distribution means for both x- and y-axis variables were statistically significantly different ($p < 0.02$) following a two-sided Student's T-test for each season and stability regime.

To test the influence of cloud shading on daytime warming, the diurnal amplitude in temperature from T_{min} to T_{max} is plotted against the measured SWD. Temperature amplitude was rarely less than 12°C when strong stability characterized the morning stratification, compared to rarely exceeding 10°C when the morning was less stable (Fig. 9e-f). The corresponding mean SWD between the morning sounding time and time when subsequent T_{max} was observed indicates more shortwave radiation was reaching the surface following the LTS > 6K cases.

To explore the daytime evolution of cloud cover following the morning LTS stratification, diurnally-averaged cloud fraction in the time window between morning sounding and time of T_{max} shows a tendency for skies to remain clear or partially cloudy following mornings with LTS > 6K (Fig. 10, blue). However, when the early morning was characterized by the less stable LTS < 2K regime, overcast cloudiness tended to persist over the course of the day, especially during winter (Fig. 10b). Consistent with a reduced (increased) cloud fraction, large (small) near-surface temperature increases are coincident with more (less) downwelling shortwave radiation reaching the surface shown in Fig. 9e-f.

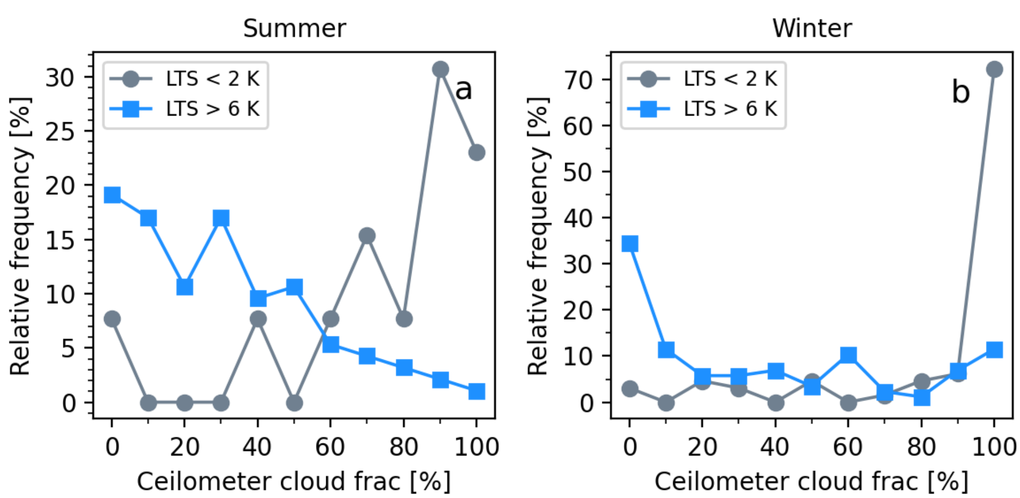

Fig. 10. Relative frequency distributions (%) of ceilometer-derived cloud fraction (%) determined between the time of 12:00 UTC radiosounding launch and the time the following day when T_{max} was reached. Distributions are shown for LTS < 2 K (gray) and LTS > 6 K (blue) stability regimes for a) summer and b) winter.

d. Radiation, turbulent heat fluxes, winds, and diurnal evolution

Distributions of sensible (SHF) and latent heat fluxes (LHF) around the morning radiosounding profile highlight different distributions depending on stability regime, revealing important process differences (Fig. 11). SHFs (reds) were negative for both stability regimes, indicating heat transfer from the atmosphere to the surface. This is consistent with the general deficits in R_{net} (Fig. 4d-e) and drop in near-surface temperature (Fig. 9c-d) as the atmosphere tries to counteract the deficit in surface energy. Despite having the same sign, medians and interquartile spreads of SHF were larger under the less stable regime than during the more stable regime. The range of SHFs associated with the weaker stability regime were frequently larger than the range of SHFs for all early morning observations (black lines), regardless of stratification. Inversely, median and spread in LHFs were positive with weaker stratification present while latent flux was essentially absent during highly stable stratification regime for both seasons. Positive LHF represents a net transport of water vapor from the surface to the atmosphere, evaporation during snow-free and sublimation during snow-covered conditions. Even though median LHF for the less regime was approximately half the magnitude of SHF, it was always in the opposite direction (from the surface to the atmosphere).

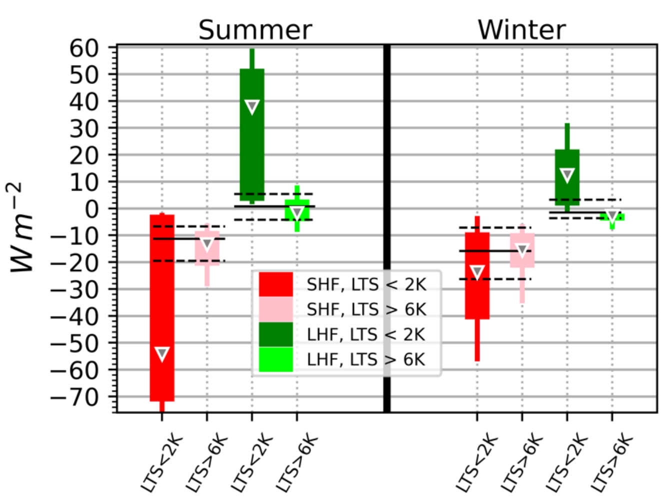

Fig. 11. Box-whisker distributions (10th-90th, 25-75th, median [triangles]) of sensible (SHF, red shades) and latent (LHF, green shades) estimated from the nearest 30-min eddy covariance turbulent heat flux averaging period to the 12:00 UTC sounding. Fluxes are separated by season and by stability regime (see x-axis). Black lines indicate the median and interquartile range of SHF and LHF for all 12:00 UTC soundings regardless of LTS for each

season. All fluxes in W m^{-2} and defined as positive upwards (transport of heat/moisture from surface to the atmosphere).

These results indicate that despite the small, yet negative radiative balance during less stable early mornings, increased heat from the atmosphere to the surface supports weak evaporation/sublimation from the surface to the atmosphere at that time. The presence of clouds, often with some amount of supercooled liquid to mitigate the occurrence of large deficits in LWN, are an important contributor to the early morning SEB. The SHFs under strongly stable stratification are weaker and less variable and corresponding LHFs were negligible. Reasons for the larger, negative SHFs under weaker stability will be discussed later in connection with near-surface winds.

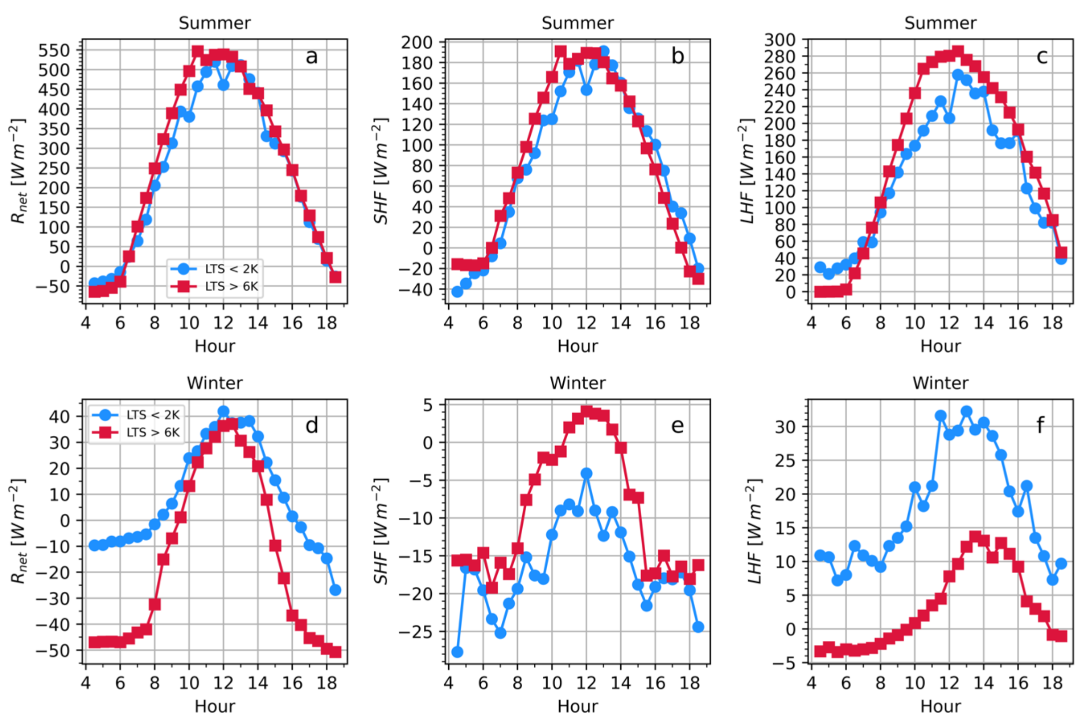

Fig. 12. Median diurnal evolution of a, d) R_{net}; b, e) SHF; and c, f) LHF for the subsequent day following the morning stability classification regime: LTS < 2 K (blue, circles) and LTS > 6 K (red, squares). Panels a-c) for summer and d-f) for winter. All fluxes in W m^{-2}.

The response of surface temperatures to radiation shown for the daytime hours following early morning stratification regimes (Fig. 9) points toward a potential preconditioning process, the link being the importance of cloud-radiative interactions on the lower atmosphere and surface thermodynamics. In Fig. 12, the daytime diurnal evolution of R_{net}, SHF, and LHF separated by morning stability regime after regime classification between 04:00-05:00 LST are presented.

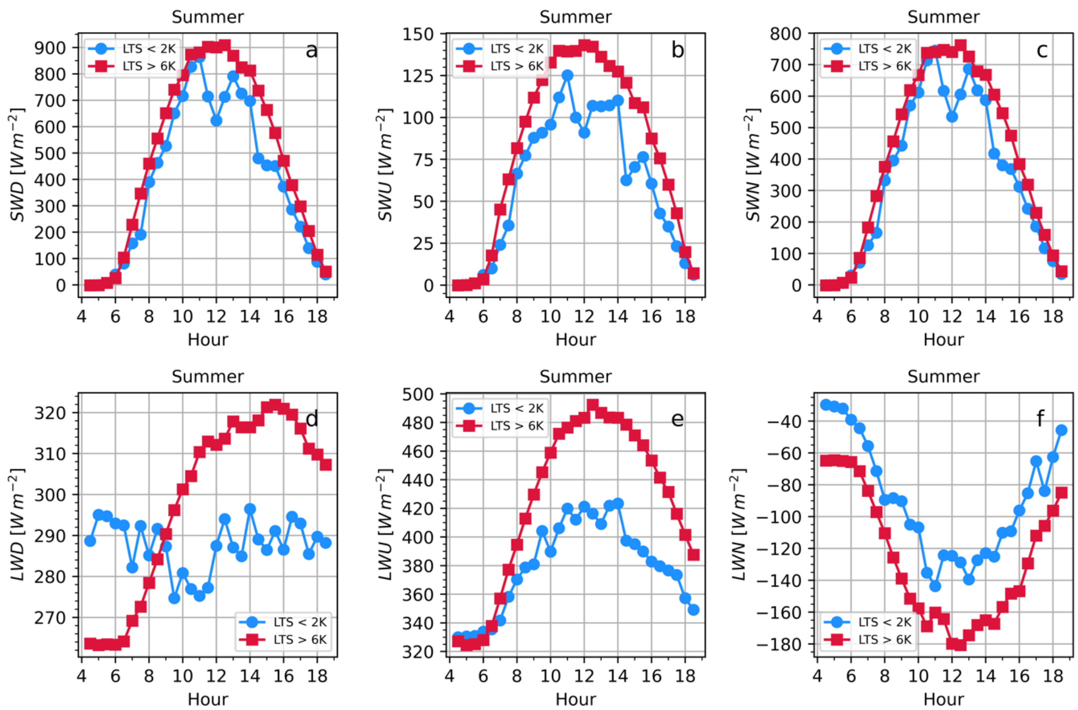

Fig. 13. Same as in Fig. 12, except for a) SWD; b) SWU; c) SWN; d) LWD; e) LWU; and f) LWN during summer.

How differences in R_{net} and the turbulent heat fluxes evolve from time of stability regime classification differed depending on the season. R_{net} is strongly dependent on the surface albedo, and the daytime absorption of solar radiation during snow-free summer (Fig. 12a) largely exceeds the solar radiation absorbed during snow-covered winter (Fig. 12d). The diurnal evolution of R_{net} is marginally larger following strong early morning stratification (red) compared to following weaker stratification (blue) in summer. But in winter, R_{net} remains slightly larger during the day for cases encountering weaker morning stability. Both

SWD and LWD critically impact R_{net} and are both largely dependent on the sky conditions (Figs. 13-14), which were shown to be persistent with the conditions of early morning sky cover (Fig. 10). Clear sky mornings supporting surface cooling and stronger stratification with the more stable regime continued to remain clear sky or have very low sky cover fractions while cloudy, less stable mornings widely remained cloudy. During summer when the surface albedo was much lower, R_{net} was dominated by SWN (Fig. 13c), which was larger with stronger stratification due to increased SWD (Fig. 13a) in connection with lower cloud fractions (Fig. 10a). In winter, SWN was small because of the high surface albedo resulted in large flux of reflected SWU, even though SWD was relatively large (Fig. 14a-c). Instead, the relative importance of LWD to R_{net} increases under the high surface albedo conditions, and it is apparent from the LWD (Fig. 14d, red) that the lack of clouds, especially low liquid-bearing clouds, causes a large deficit in LWN for the more stable regime (red) relative to the less stable regime (blue). The latter remained under the influence of higher cloud fractional occurrence of low-level clouds, seemingly retaining supercooled liquid from early morning through the subsequent day, causing both LWD and LWU to exhibit little variability as the day evolved (Fig. 14d-e, blue).

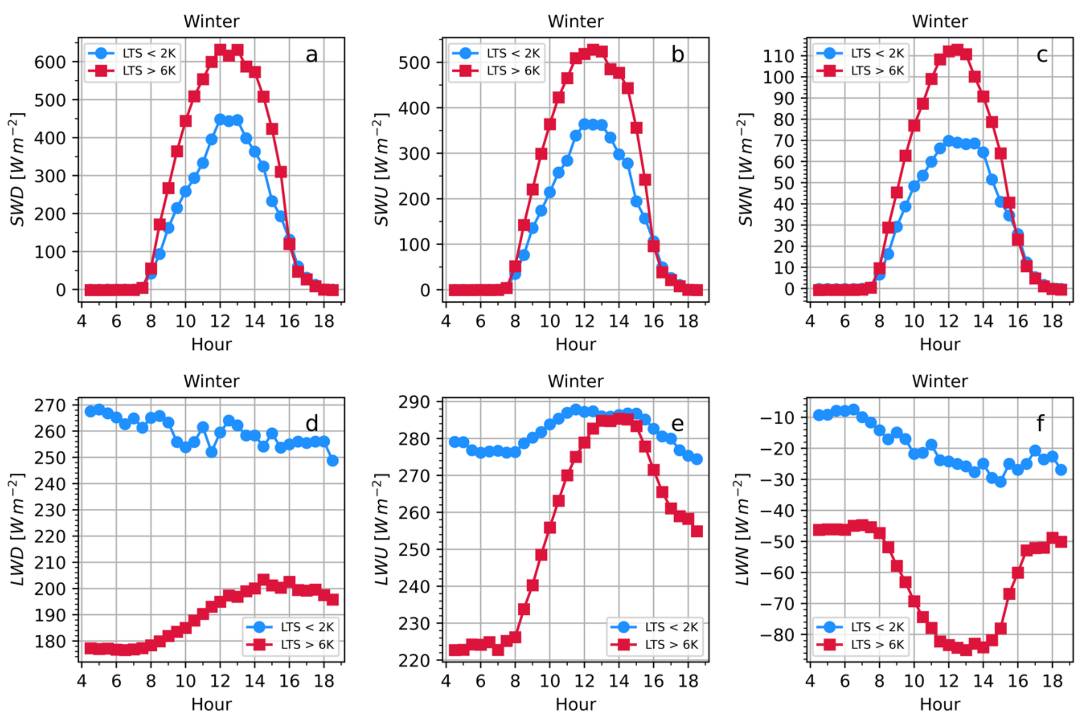

Fig. 14. Same as in Fig. 13, but for winter.

The daytime evolution of the turbulent heat fluxes showed variability depending on sky condition and morning stability regime. In summer, turbulent heat fluxes generally responded to the evolution of R_{net} (Fig. 12a-c), mimicking prototypical land-atmosphere interactions often observed during summer over relatively homogeneous land surfaces (Santanello et al., 2018; Lareau et al., 2018). In a median evolution sense, LHFs were larger than SHFs for both stability regimes, resulting in smaller Bowen ratios as the surface and vegetation respond to water availability from snowmelt.

The diurnal evolution of winter turbulent heat fluxes (THFs) (Fig. 12e-f) is where more obvious differences amongst the morning stability regimes are found. Both SHF and LHF were weaker following strong morning stability (red). Diurnal median SHF approached 0 W m^{-2} and even exceeded zero prior to mid-day (e), with LHFs also transitioning positive around the same time (f). The mid-morning timeframe is consistent with the timing of R_{net} transitioning from negative to positive (d). Adler et al. (2023) observed weak convective daytime boundary layers of approximately 200 m vertical thickness during clear sky winter days, consistent with the small but positive THFs proceeding after the strong morning stability regime. These linkages in the SEB terms are suggestive of local land-atmosphere interactions similar to those found in summer, likely in the absence of larger-scale meteorological forcing. The diurnal timing is consistent with observed wind shifts during clear sky winter days observed in Adler et al. (2023), in which they determined mountain thermal flows under quiescent conditions were responsible for down-valley to up-valley wind changes (e.g., Zardi and Whiteman, 2013). When the morning was characterized by the less stable regime (blue), the THFs experienced a different diurnal evolution. Even as R_{net} fluxes transitioned to positive around 08:00 LST, SHF remained negative throughout the day, although it did reduce in magnitude slightly by mid-morning (e). Considering the daily peak in R_{net} for winter was similar for the two stability regimes, a similar transition of negative to positive SHF would be expected if atmospheric conditions were quiescent and the land-atmosphere system were driven locally by the surface flux partitioning. That the SHFs remained negative even under weaker morning stratification suggests the weaker stability regime is predominantly forced by larger-scale synoptic features.

The corresponding LHFs remained positive (from the surface to the atmosphere) and increased throughout the day following weak morning stability (Fig. 12f, blue), reaching magnitudes approximately two to three times as large as those occurring under the strong stability regime (red). LHFs for the latter stability regime were small and negative across much of the morning, indicating a net deposition of water vapor from the atmosphere to the snow surface; water vapor deposition was not observed during the weakly stable regime, rather sublimation of snow was an ongoing process throughout the day. Using the diurnal median LHF values from the eddy covariance measurements in Fig. 12f, half-hourly sublimation rates can be calculated and accumulated to get sublimation rate per day. We estimate a sublimation rate of 0.33 mm day^{-1} when the early morning is characterized by the weaker stability regime, compared to only 0.06 mm day^{-1} for the strongly stable morning regime. This factor of five difference between regimes represents a significant amount of additional sublimation of water from the surface, a potential loss of a water resource that is no longer present in the local snowpack.

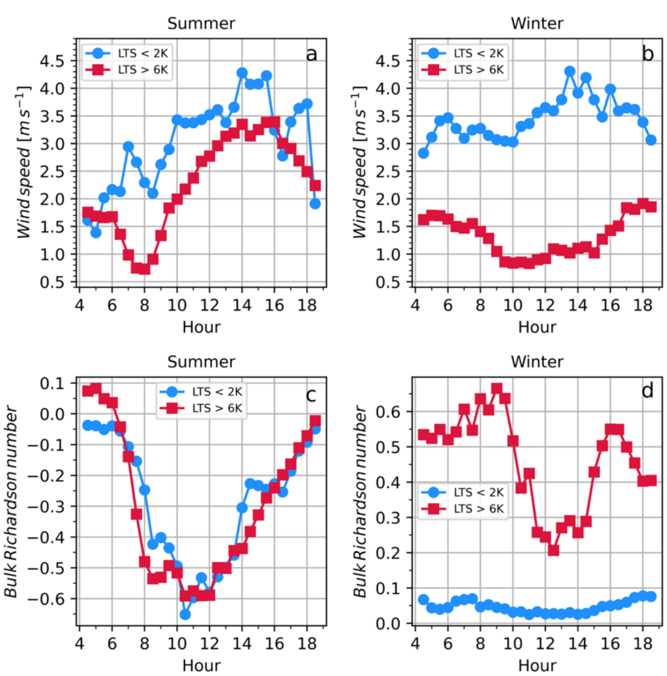

Fig. 15. a-b) Median diurnal evolution of (nominally) 3 m wind speed (m s^{-1}) following the morning stability classification regime: LTS < 2 K (blue, circles) and LTS > 6 K (red, squares) for a) summer and b) winter; c-d) median diurnal evolution of bulk Richardson number (unitless) separated by morning stability classification regime for c) summer and d) winter.

Smaller downward-directed SHF observed with the strongly stable regime relative to the weakly stable regime (Fig. 12e) is opposite to what is expected. However, near-surface wind speeds were considerably weaker when the morning was characterized by strong stability (Fig. 15a-b), especially during winter. Weaker winds in the presence of strong stability will limit the potential for mechanical mixing of statically stable air parcels downwards (Stull, 1988), and to check this, bulk Richardson numbers (Stull, 1988) were computed from wind speed and temperature measurements over the lowest 3 m AGL (Fig. 15c-d). Consistent with weaker LTS and stronger wind speeds, small Richardson numbers below the critical 0.25 value (Stull, 1988) were observed following weak morning stability (Fig. 15d, blue), suggesting any ongoing turbulent motions may continue. Oppositely, Richardson numbers remained high during the day following cases with strong early morning stratification. The relatively higher wind speeds associated with the weaker stability regime support the potential for enhanced mechanical mixing during winter (Fig. 15) and is consistent with larger (absolute) values of both SHF and LHF.

Investigating further the potential influence of synoptic forcing on winds, the diurnal evolution of predominant near-surface wind direction for winter is shown in Fig. 16. The frequency distributions reveal that a northwesterly wind direction is the predominant wind during the early morning and early evening hours, regardless of stability regime. At the Kettle Ponds location, the valley axis slopes downward in elevation from the northwest to the southeast (Fig. 1b), hence these are down-valley winds during the night. By 09:00 LST, an obvious departure in winds from the northwest is observed under the strongly stable morning regime (Fig. 16b), where the distribution shows wind directions with a more easterly component. The diurnal timing of this wind shift is broadly coincident with the surface energy budget components transitioning from negative to positive shown in Fig. 12d-f, as well as a small decrease in wind speeds (Fig. 15b). This diurnal shift in down-valley to (generally) up-valley winds is consistent with mountain thermal flows driven by pressure gradients induced from local thermal gradients due to distinct surface energy budget forcing (local) in the absence of strong wind forcing aloft (Whiteman, 1990; Whiteman and Doran, 1993; Zardi and Whiteman, 2013). While a thermal mountain flow evolution is observed for the strongly stable regime, a similar evolution is not observed under the weak stability regime (Fig. 16a). Here, the dominant nighttime flow from the northwest continues throughout the following day into early evening. A weaker, secondary peak in the distribution is seen for winds from the southeast (~120º). However, a diurnal shift in this peak is also absent, suggesting the local energy budget forcing is not contributing to a flow reversal from nighttime down-valley to daytime up-valley winds. Instead, the winds associated with this stability regime are likely forced from stronger winds aloft, which depending on their geostrophic direction relative the valley axis, can force the winds to channel along the valley axis (Whiteman and Doran, 1993). Also considering the increased wind speeds for this regime (Fig. 15b), the weakly stable, LTS < 2K, regime does not develop under predominantly quiescent conditions but rather synoptically active conditions.

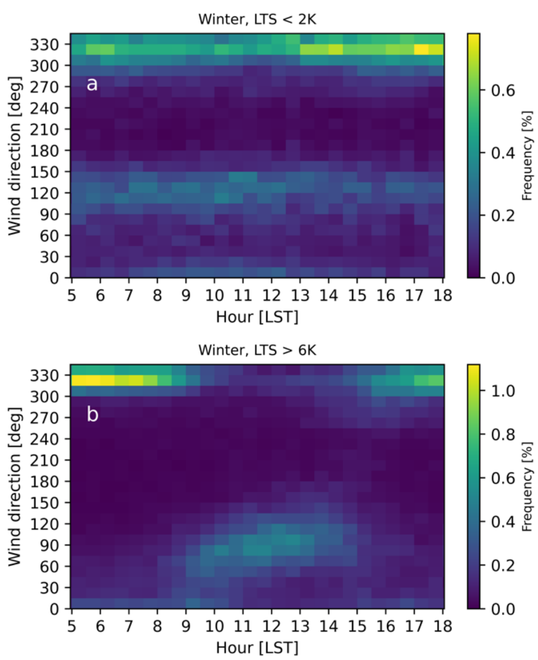

Fig. 16. Kettle Ponds near-surface wind direction (degrees) relative frequency distributions (contours, %) as a function of hour (LST) following winter-only morning sounding LTS regime classification: a) weakly stable LTS < 2K and b) strongly stable LTS > 6K.

4. Summary

Observations from coordinated but separate SAIL and SPLASH measurement campaigns, within the high-mountain East River watershed near Crested Butte, Colorado, have been analyzed to understand the relationships between clouds, surface energy forcing, and LTS. A radiative-stability bivariate metric (Sedlar et al., 2020) was used to identify two starkly different LTS regimes and their close connection to LWN. Clouds, or lack thereof, are shown to contribute to the stability structure of the lower atmosphere through associated surface radiative anomalies. During the early morning, these anomalies relative to the seasonal averages, range in energy flux of 20 to 40 W m^{-2}, and are driven by longwave radiation. The difference in R_{net} between the two stability regimes is even larger, closer to 60 W m^{-2} in summer and 50 W m^{-2} in winter. When clouds were absent or lacking highly emissive supercooled liquid, deficits in the surface R_{net} budget were enhanced through longwave loss to space causing the near-surface temperature to cool in response. Linkages between clouds, stability, and near-surface thermodynamics are similar in behavior to those noted over the high-latitude Arctic sea ice (Shupe and Intrieri, 2004; Sedlar et al., 2011; 2020; Persson, 2012, Brooks et al., 2017). However, these robust polar relationships have not yet been investigated for lower-latitude, high-mountain environments.

The "radiatively-cloudy" or "radiatively-clear" state (e.g. Stramler et al., 2011) occurring overnight and during early morning contributed to differing thermodynamic responses the following day. In the absence of cloudiness, minimum near-surface temperatures plummeted nearly 10°C cooler than when clouds were present overhead, leading to a strongly stratified lower troposphere. However, even as T_{min} was much colder during radiatively clear regime compared with radiatively cloudy, subsequent daytime T_{max} were similar between the two stability regimes. Consistent with the early morning stratification, analysis of THFs showed that both morning stability regimes were associated with downward SHFs as the lower atmosphere attempts to limit the surface energy deficit. However, the response of LHFs to these stability regimes showed that significantly larger, positive LHFs were associated with the weaker stability, radiatively cloudy regime. It is found that energy anomalies resulting during the radiatively cloudy, weaker stability regime can lead to anomalous sublimation during winter, yielding a potentially significant net loss of snowpack to the atmosphere. Further, the differences found in SEB forcing continued during the subsequent diurnal evolution. As such, the magnitude of radiative deficit and surface thermodynamic response associated with the presence or absence of radiatively clear/radiative cloudy conditions in the early morning effectively preconditioned and persisted during the subsequent day; the weakly stable regime remained highly cloudy during the day while sky conditions remained clear or partially cloudy following the strongly stable early morning regime. These cloud conditions strongly impacted the diurnal magnitude of radiative fluxes. Even as the surface albedo exceeded 80% during winter, the solar geometry of this mid-latitude mountain site means a significant fraction of downwelling radiation is still reaching the surface and driving the daytime near-surface diurnal thermodynamic evolution.

The magnitude of morning LWN during winter was shown to be dependent, to first order, upon the presence or absence of cloud cover (e.g., Fig. 6). But the presence of supercooled liquid and its impact on modifying the downwelling longwave flux over this high-mountain location has been identified as influential on the SEB (e.g., Figs. 6 and 8). While not completely exclusive, the thermodynamics impacting the cloud layers differed between stability regimes, with the less stable regime having warmer cloud base temperatures than the strongly stable regime. Taken in combination with the regime differences in near-surface wind speeds and diurnal wind shifts, it is plausible that the supercooled cloud presence is supported by larger, synoptic-scale forcing which further contributes to the weaker stability regime and the modification of the SEB through the surface longwave forcing of the clouds. On the other hand, the stronger stability regime, with relatively more clear sky or higher cloud conditions, and a defined mountain thermal flow diurnal evolution developed under relatively quiescent or very weak large-scale meteorology. A lack of longwave forcing from this regime further buffered the SEB response, permitting the surface to cool readily to space, reinforcing strong static stability across the lower troposphere.

Even small amounts of supercooled cloud liquid are shown to yield modest changes to infrared emissivity. Corresponding fluxes of LWD in the presence or absence of clouds, and cloud liquid, effectively drive the surface radiative anomalies in the high-mountain winter (e.g., Marty et al., 2002), especially when SWN is limited due to a surface that is highly reflective. Given the critical radiative forcing of these clouds, and their strong influence on lower atmosphere stratification, the process-level metrics of LWN-LTS and the results relating cloud liquid water path and radiative evolution shown here would be paramount to evaluate the capacity of numerical models in correctly representing the cloud-radiative-stability feedbacks, similar to evaluation studies over the Arctic sea ice (Pithan et al., 2014; Sedlar et al., 2020). Biases related to inadequate representation of physical process deficiencies in numerical weather prediction (e.g., Adler et al., 2023) and climate models would readily emerge using these metrics. It would be enlightening to determine whether numerical models capture the bimodality observed in the LWN-LTS space. If models are unable to represent the bimodality observed, it is likely these deficiencies will emerge from an inability resolve the cloud conditions, in particular the "radiatively cloudy" conditions, which significantly perturbs the SEB. We highly recommend the model development community implement process evaluations like those described here to assure the model physics are behaving as observed. We are currently exploring how well NOAA's operational numerical weather models represent the observed LWN-LTS relationships. In particular, we are interested in the response of the near-surface thermodynamics in relation to "radiatively cloudy" versus "radiatively clear" regimes. Further we are interested in using the weather models to classify the synoptic conditions in order to separate stability regimes by synoptically-active forcing compared with quiescent, high pressure conditions. Understanding how timescales of stratification changes during the early morning hours using higher temporal frequency remotely-sensed thermodynamic profiling observations and the comparison with models is also a target of future study.

Acknowledgments.

The authors wish to thank all personnel involved in developing the observing systems, deploying instrumentation, and data communications and quality assurance. In particular, we thank Emiel Hall, Christian Herrera, Gary Hodges, Logan Soldo, and Scott Stierle from the NOAA Global Monitoring Laboratory and CIRES at the University of Colorado Boulder. We also thank the NOAA Air Resources Laboratory for their efforts in deploying and maintaining he flux tower operations. A special thank you is extended to Erik Hulm and Benn Schmatz at RMBL for all their year-round support of our instruments during the SPLASH campaign. This research has been supported in part by funding from NOAA cooperative agreements NA17OAR4320101 and NA2OAR4320151, Department of Energy's

Atmospheric Systems Research Award Number DE-SC0024266, the NOAA Atmospheric Science for Renewable Energies program, and the NOAA Physical Sciences Laboratory.

Data Availability Statement.

All observed data sets used in this study are freely available to the public. Measurements the SAIL Atmospheric Radiation Measurement (ARM) Mobile Facility (AMF2) used include the balloon-based radiosounding profiles (Atmospheric Radiation Measurement (ARM) user facility, 2021a), the microwave radiometer (MWR) retrieved liquid water paths (LWP) (Atmospheric Radiation Measurement (ARM) user facility, 2021b), and HSRL (Atmospheric Radiation Measurement (ARM) user facility, 2023) at Gothic. NOAA Global Monitoring Laboratory produced the radiation budget and near-surface temperature and wind speed and direction measurements from Kettle Ponds (Soldo et al., 2023) and ceilometer measurements and retrievals of cloud fractional occurrence and cloud base height (Telg et al., 2024). NOAA Air Resources Laboratory provided sensible and latent heat flux measurements from Kettle Ponds (NOAA Air Resources Laboratory, 2021).

REFERENCES

Adler, B., and Coauthors, 2023: Impact of seasonal snow-cover change on the observed and simulated state of the atmospheric boundary layer in a high-altitude mountain valley, *J. Geophys. Res. Atmos.*, 128, e2023JD038497. https://doi.org/10.1029/2023JD038497.

Atmospheric Radiation Measurement (ARM) user facility, 2021a: Balloon-Borne Sounding System (SONDEWNPN). 2021-09-01 to 2023-06-16, ARM Mobile Facility (GUC) Gunnison, CO; AMF2 (main site for SAIL) (M1). Compiled by E. Keeler, K. Burk, and J. Kyrouac. ARM Data Center. Data set accessed 2023-07-08 at http://dx.doi.org/10.5439/1595321.

Atmospheric Radiation Measurement (ARM) user facility, 2021b: Microwave Radiometer (MWRLOS). 2021-09-01 to 2023-06-16, ARM Mobile Facility (GUC) Gunnison, CO; AMF2 (main site for SAIL) (M1). Compile by M. Cadeddu and M. Tuftedal. ARM Data Center. Data set accessed 2023-07-19 at http://dx.doi.org/10.5439/1046211.

Atmospheric Radiation Measurement (ARM) user facility, 2023: High Spectral Resolution Lidar (hsrl). 2021-09-01 to 2023-06-15, ARM Mobile Facility (GUC) Gunnison, CO; AMF2 (main site for SAIL) (M1). Compiled by R. Bambha, E. Eloranta, J. Garcia, and B. Ermold. Data set accessed 2023-11-29 at http://dx.doi.org/10.5439/1462207.

Brooks, I. M., and Coauthors, 2017: The Turbulent Structure of the Arctic Summer Boundary Layer During The Arctic Summer Cloud-Ocean Study, *J. Geophys. Res. Atmos.*, 122, 9685-9704, https://doi.org/10.1002/2017JD027234.

Ceppi, P. and P. Nowack, 2021: Observational evidence that cloud feedback amplifies global warming, *PNAS*, 118, No. 30, https://doi.org/10.1073/pnas.2026290118.

Curry, J. A., W. B. Rossow, D. Randall, and J. L Schramm, 1996: Overview of Arctic Cloud and Radiation Characteristics, *J. Clim.*, 9, 1731-1764, https://doi.org/10.1175/1520-0442(1996)009<1731:OOACAR>2.0.CO;2.

de Boer, G., and Coauthors, 2023: Supporting Advancement in Weather and Water Prediction in the Upper Colorado River Basin: The SPLASH Campaign, *Bull. Amer. Meteorol. Soc.*, E1853-E1874, https://doi.org/10.1175/BAMS-D-22-0147.1.

Eloranta, E. W., 2005: High Spectral Resolution Lidar. In: Lidar: Range-Resolved Optical Remote Sensing of the Atmosphere, Wietkamp, K. (eds.), Springer-Verlag, New York.

Engström, A., J. Karlsson, and G. Svensson, 2014: The Importance of Representing Mixed-Phase Clouds for Simulating Distinctive Atmospheric States in the Arctic, *J. Climate*, 27, 265-272, https://doi.org/10.1175/JCLI-D-13-00271.1.

Feldman, D. R. and Coauthors, 2023: The Surface Atmosphere Integrated Field Laboratory (SAIL) Campaign, *Bull. Amer. Meteorol. Soc.*, E2192-E222, https://doi.org/10.1175/BAMS-D-22-0049.1.

Inoue, J. and K. Sato, 2023: Comparison of the depolarization measurement capability of a lidar ceilometer with cloud particle sensor sondes: a case study of liquid water clouds, *Polar Science*, 35, 100911, https://doi.org/10.1016/j.polar.2022.100911.

Intrieri, J. M., C. W. Fairall, M. D. Shupe, P. O. G. Persson, E. L. Andreas, P. S. Guest, and R. E. Moritz, 2002a: An annual cycle of Arctic surface cloud forcing at SHEBA, *J. Geophys. Res.*, 107, C10, 8039, https://doi.org/10.1029/2000JC000439.

Intrieri, J. M., M. D. Shupe, T. Uttal, and B. J. McCarty, 2002b: An annual cycle of Arctic cloud characteristics observed by radar and lidar at SHEBA, *J. Geophys. Res.*, 107, C10, 8030, https://doi.org/10.1029/2000JC000423.

Jin, M. and S. Liang, 2006: In Improved Land Surface Emissivity Parameter for Land Surface Models Using Global Remote Sensing Observations, *J. Climate*, 19, 2867-2881, https://doi.org/10.1175/JCLI3720.1.

Lareau, N. P., Y. Zhang, and S. A. Klein, 2018: Observed Boundary Layer Controls on Shallow Cumulus at the ARM Southern Great Plains Site, *J. Atmos. Sci.*, 75, 2235-2255, https://doi.org/10.1175/JAS-D-17-0244.1.

Marty, Ch., R. Philipona, C. Frölich, and A. Ohmura, 2002: Altitude dependence of surface radiation fluxes and cloud forcing in the alps: results from the alpine surface radiation budget network, *Theor. Appl. Climatol.*, 72, 137-155, https://doi.org/10.1007/s007040200019.

Miller, N. B., M. D. Shupe, C. J. Cox, V. P Walden, D. D. Turner, and K. Steffen, 2015: Cloud Radiative Forcing at Summit, Greenland, *J. Climate*, 28, 6267-6280, https://doi.org/10.1175/JCLI-D-15-0076.1.

Morrison, H., G. de Boer, G. Feingold, J. Harrington, M. D. Shupe, and K. Sulia, 2012: Resilience of persistent Arctic mixed-phase clouds, *Nature Geosci.*, 5, 11-17, https://doi.org/10.1038/NGEO1332.

NOAA Air Resources Laboratory, 2021: Flux Data at Kettle Ponds. http://ftp.arl.noaa.gov/pub/GEWEX/SPLASH.

Ohmura, A., 2001: Physical Basis for the Temperature-Based Melt-Index Model, *J. Appl. Meteorol.*, 753-761, 2001, https://doi.org/10.1175/1520-0450(2001)040<0753:PBFTTB>2.0.CO;2.

Paluch, I. R. and D. H. Lenschow, 1991: Stratiform Cloud Formation in the Marine Boundary Layer, *J. Atmos. Sci.*, 2141-2158, https://doi.org/10.1175/1520-0469(1991)048<2141:SCFITM>2.0.CO;2.

Peixoto, J. P. and A. H. Oort, 1992: *Physics of Climate*. American Institute of Physics, New York, USA, 520 pp.

Persson, P. O. G., 2012: Onset and end of the summer melt season over sea ice: thermal structure and surface energy perspective from SHEBA, *Clim. Dyn.*, 39, 1349-1371, https://doi.org/10.1007/s00382-011-1196-9.

Pithan, F., B. Medeiros, and T. Mauritsen, 2014: Mixed-phase clouds cause climate model biases in Arctic wintertime temperature inversions, *Clim. Dyn.*, 43, 289-303, https://doi.org/10.1007/s00382-013-1964-9.

Ramanathan, V., R. D., Cess, E. F. Harrison, P. Minnis, B. R. Barkstrom, E. Ahmad, and D. Hartmann, 1989: Cloud-Radiative Forcing and Climate: Results from the Earth Radiation Budget Experiment, *Science*, 243, 57-63, https://doi.org/10.1126/science.243.4887.57.

Santanello Jr., J. A., and coauthors, 2018: Land-Atmosphere Interactions. The LoCo Perspective, *Bull. Amer. Meteorol. Soc.*, 99 (6), 1253-1272, https://doi.org/10.1175/BAMS-D-17-0001.1.

Sedlar, J. and R. Hock, 2009: Testing longwave radiation parameterizations under clear and overcast skies at Storglaciären, Sweden, *The Cryosphere*, 3, 75-84, https://doi.org/10.5194/tc-3-75-2009.

Sedlar, J. and Coauthors, 2011: A transitioning Arctic surface energy budget: the impacts of solar zenith angle, surface albedo and cloud radiative forcing, *Clim. Dyn.*, 37, 1643-1660, https://doi.org/10.1007/s00382-010-0937-5.

Sedlar, J., 2014: Implications of Limited Liquid Water Path on Static Mixing within Arctic Low-Level Clouds, *J. Appl. Meteorol. Climatol.*, 53, 2775-2789, https://doi.org/10.1175/JAMC-D-14-0065.1.

Sedlar, J. and M. D. Shupe, 2014: Characteristic nature of vertical motions observed in Arctic mixed-phase stratocumulus, *Atmos. Chem. Phys.*, 14, 3461-3478, https://doi.org/10.5194/acp-14-3461-2014.

Sedlar, J., 2018: Spring Arctic Atmospheric Preconditioning: Do Not Rule Out Shortwave Radiation Just Yet, *J. Climate*, 31, 4225-4240, https://doi.org/10.1175/JCLI-D-17-0710.1.

Sedlar, J., and Coauthors, 2020: Confronting Arctic Troposphere, Clouds, and Surface Energy Budget Representations in Regional Climate Models With Observations, *J. Geophys. Res. Atmos.*, 124, https://doi.org/10.1029/2019JD031783.

Shupe, M. D., 2007: A ground-based multisensory cloud phase classifier, *Geophys. Res. Lett.*, 34, L22809, https://doi.org/10.1029/2007GL031008.

Shupe, M. D. and J. M. Intrieri, 2004: Cloud Radiative Forcing of the Arctic Surface: The Influence of Cloud Properties, Surface Albedo, and Solar Zenith Angle, *J. Climate*, 17, 616-628, https://doi.org/10.1175/1520-0442(2004)017<0616:CRFOTA>2.0.CO;2.

Shupe, M. D., P. Kollias, P. O. G. Persson, and G. M. McFarquhar, 2008: Vertical Motions in Arctic Mixed-Phase Stratiform Clouds, *J. Atmos. Sci.*, 65, 1304-1322, https://doi.org/10.1175/2007JAS2479.1.

Shupe, M. D., P. O. G. Persson, I. M. Brooks, M. Tjernström, J. Sedlar, T. Mauritsen, S. Sjogren, and C. Leck, 2013: Cloud and boundary layer interactions over the Arctic sea ice in late summer, *Atmos. Chem. Phys.*, 13, 9379-9400, https://doi.org/10.5194/acp-13-9379-2013.

Skiles, S. M., T. H. Painter, J. S. Deems, A. C. Bryant, and C. C. Landry, 2012: Dust radiative forcing in snow of the Upper Colorado River Basin: 2. Interannual variability in radiative forcing and snowmelt rates, *Water Resources Res.*, 48, W07522, https://doi.org/10.1029/2012WR011986.

Skiles, S. M., M. Flanner, J. M. Cook, M. Dumont, and T. H. Painter, 2018: Radiative forcing by light-absorbing particles in snow, *Nature Clim. Change*, 8, 964-971, https://doi.org/10.1038/s41558-018-0296-5.

Soldo, L., S. Stierle, D. Hageman, E. Hall, C. Herrera, G. Hodges, K. Lantz, L. Riihimaki, and J. Sedlar, 2023: NOAA GML Kettle Ponds Surface Radiation Budget and Near-Surface Meteorology Data for SPLASH (v.1.1) [Data set]. Zenodo. https://doi.org/10.5281/zenodo.8432741.

Sotiropoulou, G., and Coauthors, 2016: Atmospheric Conditions during the Arctic Clouds in Summer Experiment (ACSE): Contrasting Open Water and Sea Ice Surfaces during Melt and Freeze-Up Seasons, *J. Climate*, 29, 8721-8744, https://doi.org/10.1175/JCLI-D-16-0211.1.

Stephens, G. L., 1978a: Radiation Profiles in Extended Water Clouds. I: Theory, *J. Atmos. Sci.*, 35, 2111-2122, https://doi.org/10.1175/1520-0469(1978)035<2111:RPIEWC>2.0.CO;2.

Stephens, G. L., 1978b: Radiation Profiles in Extended Water Clouds. II: Parameterization Schemes, *J. Atmos. Sci.,* 35, 2123-2132, https://doi.org/10.1175/1520-0469(1978)035<2123:RPIEWC>2.0.CO;2.

Stramler, K., A. D. Del Genio, and W. B. Rossow, 2011: Synoptically Driven Arctic Winter States, *J. Climate*, 24, 1747-1762, https://doi.org/10.1175/2010JCLI3817.1.

Stull, R. B., 1988: *An Introduction to Boundary Layer Meteorology*. Kluwer Academic Publishers, Dordrecht, The Netherlands, 666 pp.

Telg, H., J. Sedlar, C. Herrera, and S. Stierle, 2024: NOAA GML and CIRES/Uni. Of Colorado-Boulder Ceilometer Cloud Data Products at Kettle Ponds (CKP) for SPLASH (1.3.2) [Data set]. Zenodo. https://doi.org/10.5281/zenodo.10520198.

Walsh, J. E. and W. L. Chapman, 1998: Arctic Cloud-Radiation-Temperature Associations in Observational Data and Atmospheric Reanalyses, *J. Climate*, 11, 3030-3045, https://doi.org/10.1175/1520-0442(1998)011<3030:ACRTAI>2.0.CO;2.

Weihs, P., J. Laimighofer, H. Formayer, and M. Olefs, 2021: Influence of snow making on albedo and local radiative forcing in an alpine area, *Atmos. Res.*, 255, https://doi.org/10.1016/j.atmosres.2020.105448.

Westwater, E. R., Y. Han, M. D. Shupe, and S. Y. Matrosov, 2001: Analysis of integrated cloud liquid and precipitable water vapor retrievals from microwave radiometers during the Surface Heat Budget of the Arctic Ocean project, *J. Geophys. Res.*, 106, D23, 32019-32030, https://doi.org/10.1029/2000JD000055.

Whiteman, C. D., 1990: Observations of Thermally Developed Wind Systems in Mountainous Terrain. In: Blumen, W. (eds) Atmospheric Processes over Complex Terrain. Meteorological Monographs, 23, Amer. Meteorol., Soc., Boston, MA. https://doi-org.colorado.idm.oclc.org/10.1007/978-1-935704-25-6_2.

Whiteman, C. D. and J. C. Doran, 1993: The Relationship between Overlying Synoptic-Scale Flows and Winds within a Valley, *J. Appl. Meteorol.*, 32, 1669-1682.

Wood, R. and C. S. Bretherton, 2006: On the Relationship between Stratiform Low Cloud Cover and Lower-Tropospheric Stability, *J. Climate*, 19, 6425-6432, https://doi.org/10.1175/JCLI3988.1.

Zardi, D. and C. D. Whiteman, 2013: Diurnal Mountain Wind Systems. In: Chow, F., De Wekker, S., Snyder, B. (eds.) Mountain Weather Research and Forecasting. Springer Atmospheric Sciences. Spring, Dordrecht.